Draft version April 21, 2026
Typeset using LaTeX **twocolumn** style in AASTeX7.0.1

Pulsational mass loss from supermassive stars creates the compact shells of Little Red Dots

Devesh Nandal,[1] Igor V. Chilingarian,[1] Chris Nagele,[2] John Chisholm,[3,4] Franz E. Bauer,[5] and Abraham Loeb[1]

[1] *Center for Astrophysics, Harvard and Smithsonian, 60 Garden St, Cambridge, MA 02138, USA*
[2] *Department of Physics and Astronomy, Johns Hopkins University, Baltimore MD 21218, USA*
[3] *Department of Astronomy, The University of Texas at Austin, Austin, TX 78712, USA*
[4] *Cosmic Frontier Center, The University of Texas at Austin, Austin, TX 78712, USA*
[5] *Instituto de Alta Investigación, Universidad de Tarapacá, Casilla 7D, Arica, 1010000, Chile*

ABSTRACT

Little Red Dots (LRDs) have emerged as one of the central puzzles of the JWST era. Their spectra increasingly require dense gas close to the source, yet the physical origin of that cocoon-like structure remains unclear. We examine whether late pulsational mass loss from supermassive stars (SMS) leads to dense gas cocoons. We analyze five GENEC models at different metallicities with characteristic masses of order $10^5\,M_\odot$, following them through post-accretion evolution with radial pulsation calculations and general relativistic (GR) stability diagnostics. Mass loss during the final stages of evolution occurs not as a steady wind, but through discrete strange-mode ejection episodes. In the $Z = 10^{-2}\,Z_\odot$ model, four late episodes last 41–282 yr and eject 10–348 $M_\odot$ each, for a total loss of $(4.8-10)\times10^2\,M_\odot$; the final episode alone contributes $\simeq 73\%$ of that budget. Since the last episode dominates the mass-loss, it is the only event sufficiently massive enough to leave behind a compact, optically thick shell extending out to 0.4 pc that reproduces the LRD dense gas cocoon. Final ejecta are H/He dominated but chemically distinctive, with a robust nitrogen-rich composition, $\log(\mathrm{N/O}) \simeq 0.13$ and $\log(\mathrm{C/O}) \simeq -0.23$. SMS reaches GR instability at an age of ~ 1 Myr and collapses in $\sim 10^4$ s, retaining $\sim 99\%$ all of its mass. Across the full metallicity range from Pop III to $10^{-2}\,Z_\odot$, this shell-ejection channel persists. SMSs therefore provides a physically motivated origin for the compact cocoon-like structure implied by LRDs, while remaining the natural progenitors of the massive black hole seeds invoked in direct collapse scenario.

Keywords: early universe — dark ages, reionization, first stars — galaxies: formation — galaxies: high-redshift

1. INTRODUCTION

The existence of $\gtrsim 10^9\,M_\odot$ black holes within the first billion years remains a demanding constraint on models of seed formation in the early universe, and JWST has now placed this problem in a new observational context. Supermassive stars provide one of the clearest routes to heavy seeds because their collapse can occur from progenitors that already reach $\sim 10^5\,M_\odot$, avoiding the need for prolonged super-Eddington growth from light remnants. Early work established the basic structure and stability of radiation-dominated stars and clarified how relativistic instability can drive their collapse (F. Hoyle & W. A. Fowler 1963; S. Chandrasekhar 1964; W. A. Fowler 1966; I. Appenzeller & K. Fricke 1972; G. M. Fuller et al. 1986). More recent studies showed that rapid accretion can assemble stars of 10^4–$10^6\,M_\odot$ and revived SMSs as plausible progenitors of heavy black-hole seeds (V. Bromm & A. Loeb 2003; M. C. Begelman et al. 2006; T. Hosokawa et al. 2012a; Y. Sakurai et al. 2015; T. E. Woods et al. 2017; L. Haemmerlé et al. 2018). Related work has also broadened the environments in which such objects may form, including dense stellar systems and mildly enriched gas (J. A. Regan et al. 2020; J. H. Wise et al. 2019; B. Reinoso et al. 2023; D. Nandal et al. 2024a, 2025a).

JWST has given this problem a new observational setting through the discovery of Little Red Dots (LRDs), a population of compact high-redshift sources with red rest-optical continua, broad Balmer emission, and

Corresponding author: Devesh Nandal
deveshnandal@yahoo.com

prominent spectral structure around the Balmer break (L. J. Furtak et al. 2023; Y. Harikane et al. 2023; J. Matthee et al. 2024; D. D. Kocevski et al. 2025; H. B. Akins et al. 2025; A. de Graaff et al. 2025a; D. J. Setton et al. 2025; R. P. Naidu et al. 2025). A growing body of work now points to dense gas close to the source as a central ingredient in shaping both the continuum and the emission-line appearance of at least part of the LRD population (J. F. W. Baggen et al. 2024; K. Inayoshi & R. Maiolino 2025; X. Ji et al. 2025; V. Rusakov et al. 2026; V. Kokorev et al. 2025; Y. Asada et al. 2026; J. Matthee et al. 2026). This has shifted attention not only to the nature of the central engine, but also to the origin of the compact circumsource material, it's stability, evolution, time-scales, and survivability itself. Any SMS-based interpretation must therefore explain how dense gas can be placed on compact scales and the kinematics at the stage when the source becomes observable as an LRD, rather than treating that material as an external assumption (K. Inayoshi & R. Maiolino 2025; A. de Graaff et al. 2025b; R. Maiolino et al. 2025).

Recent studies have shown that SMS spectra can reproduce several defining LRD features, while other models invoke SMSs embedded in massive self-gravitating accretion structures (L. Zwick et al. 2025; D. Nandal & A. Loeb 2026; J. Chisholm et al. 2026). However, a key remaining question is whether SMSs can also produce the surrounding gas required by these interpretations. Pulsational mass loss offers one possible channel. The envelopes of luminous radiation-dominated stars are prone to strongly nonadiabatic strange-mode instability, and related pulsations have long been studied in massive stars and supergiants (M. Kiriakidis et al. 1993; W. Glatzel 1994; H. Saio et al. 1998; M. Godart et al. 2011; H. Saio et al. 2013; T. Sonoi & H. Shibahashi 2014; A. P. Yadav et al. 2018). In the SMS context, most previous work has focused on whether pulsations limit continued growth during rapid accretion, or on how instability develops as the star approaches relativistic collapse (K. Inayoshi et al. 2013; D. Nakauchi et al. 2020; H. Saio et al. 2024). Much less attention has been given to whether late pulsational episodes can expel weakly bound envelope material and thereby explain the compact shell with properties relevant to LRD phenomenology.

In this Letter, we test the following scenario for the Balmer-break/LRD regime. After accretion ends, the SMS contracts, ignites hydrogen burning, and reexpands into a phase of strange-mode instability. A small number of discrete pulsational ejections then remove weakly bound envelope material and build a compact dense cocoon with a characteristic composition around the star. The SMS itself continues evolving toward GR instability and later collapses into a heavy black-hole seed. Section 2 describes the stellar models and pulsation framework. Section 3 presents the resulting mass-loss episodes, shell properties, and ejecta composition. Section 4 discusses the implications for LRDs and heavy-seed formation and section 5 summarizes our findings.

2. METHODS

2.1. *Stellar models*

We analyse five accreting GENEC SMS models spanning $Z/Z_\odot = 0$, 10^{-5}, 10^{-4}, 10^{-3}, and 10^{-2}. Each sequence begins from a fully convective $10\,M_\odot$ seed and grows at a near-constant accretion rate of $\dot{M} = 1\,M_\odot\,\mathrm{yr}^{-1}$ to a characteristic mass of order $10^5\,M_\odot$. The models are then followed through their post-accretion evolution. We use the advanced GENEC nuclear network (D. Nandal & S. Chon 2026), which follows species up to the Fe group, and each stored structure contains more than 1200 radial layers.

Our pulsation analysis uses every available stored model along each sequence. Additional details of the input structure, preprocessing, and quality checks are given in Appendix A.

2.2. *Radial pulsations and episodic mass loss*

The envelopes of SMSs are luminous, weakly bound, and strongly radiation dominated (T. Hosokawa et al. 2012b; T. E. Woods et al. 2020). Strange modes are envelope-confined pulsations that arise in stars with high L/M and short thermal times in their outer layers. Unlike ϵ-modes, which are tied to nuclear burning, or κ-modes, which rely on opacity driving, strange modes are favored when radiation pressure and rapid radiative diffusion alter the usual phase relation between pressure and density in the outer envelope. SMSs naturally enter this regime, so strongly nonadiabatic surface layers can support strange-mode behaviour (H. Saio et al. 1998, 2013; T. Sonoi & H. Shibahashi 2014). We therefore solve the linear adiabatic radial problem in Newtonian gravity for the lowest few modes of each stored model, and also carry out a complementary general-relativistic radial calculation following H. Saio et al. (2024). The Newtonian modes provide the default eigenfunctions for the later analysis, while the GR calculation tracks the approach to GR instability.

We then evaluate driving and damping on these adiabatic eigenfunctions, rather than solving the full complex nonadiabatic problem. This quasi-nonadiabatic step provides a growth proxy. Physically, it asks whether the radiative envelope does net positive work on the oscillation over a cycle, so that the mode gains energy and

grows, or instead loses more energy to damping than it receives from driving:

$$E_{\rm mode} = \int \frac{1}{2}\rho\omega_r^2\xi_r^2\, dV, \qquad \gamma = \frac{1}{2E_{\rm mode}}\int \dot{p}_{\rm tot}\, dV, \tag{1}$$

where $E_{\rm mode}$ is the mode energy, ρ the local density, ω_r the real mode frequency, ξ_r the radial displacement eigenfunction, and $\dot{p}_{\rm tot}$ the local work rate per unit volume from all driving and damping contributions. The quantity γ measures the corresponding net growth rate.

We then map the inferred driving through energy conservation and pulsation-linked mass-loss estimate,

$$\dot{M} = \frac{2\eta L_{\rm drive}}{v_{\rm esc,eff}^2}, \tag{2}$$

and cap each estimate by the mass accessible above the inferred driving region. We do not interpret these values as steady winds. Instead, we group unstable models into discrete ejection episodes and derive the mass-loss histories, launch conditions, and shell properties used below. Full diagnostics and assumptions are given in Appendix A.

2.3. *GR stability and collapse follow-up*

We assess the final fate of the models with complementary GR stability diagnostics (H. Saio et al. 2024; L. Haemmerlé 2021a; C. Nagele et al. 2022), and remap unstable snapshots to a 1D GR hydrodynamics code with a 52-isotope nuclear network and neutrino cooling (C. Nagele et al. 2021). In the baseline calculation, the unstable SMS proceeds to black-hole formation rather than disruption. Further details of the GR criteria, snapshot selection, and collapse evolution are given in Appendix A.11 and A.12 .

3. RESULTS

Figure 1 summarizes the evolutionary picture that emerges from our analysis. After accretion ends, the SMS contracts, ignites hydrogen burning, and re-expands into a late phase of strange-mode instability. In this phase, pulsation-driven mass loss occurs through a small number of discrete shell ejections. The earlier ejections expand to large radii, while the final pre-collapse ejection remains compact, optically thick, chemically distinctive, and therefore sets the immediate circumstellar environment relevant to the LRD phase. The SMS then continues to GR instability and ultimately collapses into a heavy black-hole seed. In the rest of this section, we quantify this sequence and identify which ejection episode dominates the circumstellar environment at collapse.

Of the five models in our grid, we focus first on the $Z = 10^{-2}\,Z_\odot$ model, which is the closest match to the low but non-zero metallicity regime often associated with LRDs and their nearby analogues. No radiative-wind prescription is imposed, so the mass loss discussed below is entirely pulsational. The accreting phase is pulsationally quiet and is not pursued further here; a fuller account of the pre-main sequence is given in D. Nandal et al. (2023, 2025b); D. Nandal & A. Loeb (2026).

3.1. *Post-accretion evolution of the $Z = 10^{-2}\,Z_\odot$ model*

The post-accretion track is shown in the left panel of Fig. 2, where color encodes the declining central H mass fraction. Once accretion ends, the inflated envelope is no longer maintained, and the star contracts on a Kelvin–Helmholtz timescale. The track moves blueward from $\log(L/L_\odot) = 9.57$ and $\log T_{\rm eff} = 3.92$ to a maximum temperature of $\log T_{\rm eff} = 4.32$ at nearly unchanged luminosity, $\log(L/L_\odot) = 9.55$. This contraction lasts $\simeq 1.35 \times 10^5$ yr and remains entirely free of pulsation-driven mass loss.

The contraction ends at $X_{\rm c} \simeq 0.69$, where the track bends back to the red. By then the energy budget is dominated by CNO burning, and the track migrates to lower $T_{\rm eff}$ again as the outward flux does work in expanding the envelope (D. Nandal et al. 2023, 2024b; D. Nandal & A. Loeb 2026). The star therefore returns to a red-supergiant-like configuration, not on the short thermal timescale of the earlier contraction, but on the much slower nuclear timescale. Over the next $\sim 9 \times 10^5$ yr it evolves to $\log(L/L_\odot) = 9.57$, $\log T_{\rm eff} = 3.90$, and age 1.1 Myr, by which point the central H fraction has fallen to $X_{\rm c} \simeq 0.10$. During this re-expansion, the inflated radiation-dominated envelope becomes increasingly weakly bound, while the outer layers remain strongly nonadiabatic, favoring strange-mode driving. The first three pulsation-driven mass loss episodes appear along this long redward drift, marked by the purple segments in the left panel of Fig. 2.

The final stage is spent at near constant effective temperature highlighted in the same panel. From 1.10 to 1.27 Myr, the star remains in this region and undergoes its fourth, and final, pulsation-loss episode. By age 1.27 Myr, when $X_{\rm c} \simeq 0.01$, the model satisfies the GR instability criterion and enters dynamical collapse. Despite this large excursion across the HR diagram, the luminosity stays confined to the narrow range $\log(L/L_\odot) = 9.55$–9.57 along the full post-accretion track.

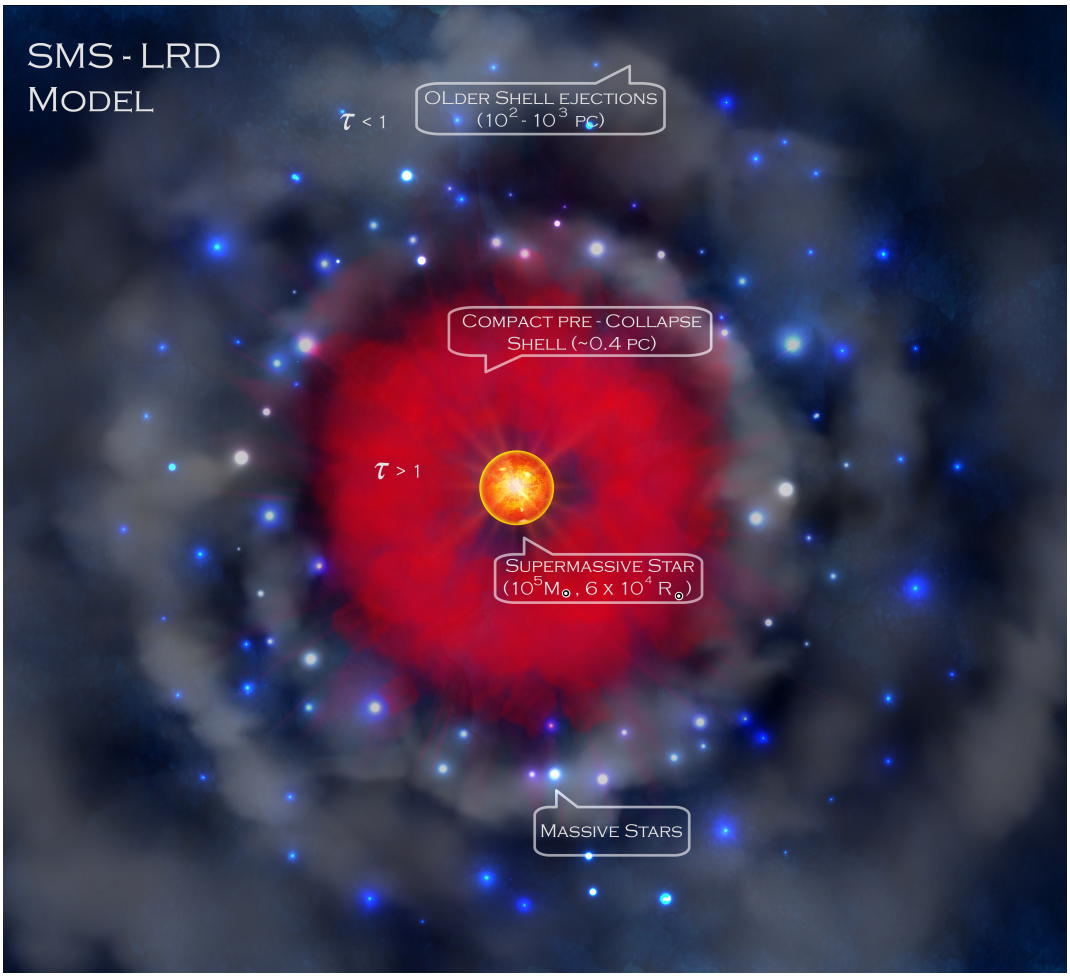

Figure 1. Schematic illustration of the SMS pathway explored in this Letter, from the end of accretion to collapse. After accretion ends, the star contracts, ignites hydrogen burning, and re-expands into a late phase of strange-mode instability. Pulsation-driven mass loss then proceeds through discrete ejection episodes that remove weakly bound envelope material. The earlier shells expand to large radii, whereas the final pre-collapse ejection remains compact and dense, setting the immediate circumstellar environment relevant to the LRD phase. The ejecta also carries a characteristic abundance pattern. The SMS then continues toward GR instability and ultimately collapses into a heavy black-hole seed. The drawing is schematic and not to scale.

3.2. *Pulsation-driven mass-loss history*

The four purple windows in the left panel of Fig. 2 map directly onto the four discrete ejection episodes in the right panel, centered at 0.322, 0.520, 0.959, and 1.218 Myr. The mass loss is therefore highly selective in time. It is not spread smoothly across the post-accretion evolution, but concentrated into several well-separated outbursts.

The right panel of Fig. 2 shows that the strength of these events rises systematically with time. On the fiducial branch, the mean mass-loss rates increase from 0.25 and 0.32 $M_\odot\,\mathrm{yr}^{-1}$ in the first two episodes to 0.67 and 1.23 $M_\odot\,\mathrm{yr}^{-1}$ in the third and fourth. The upper branch follows the same progression, with rates of 0.84, 1.08, 2.25, and 2.13 $M_\odot\,\mathrm{yr}^{-1}$. The effective durations of each episode also lengthen from 41.1 and 60.6 yr to 151.2 and 281.9 yr. The late episodes are therefore stronger both in their instantaneous rates and in their finite durations.

The same pattern appears even more clearly in the integrated ejecta masses in the bottom window of the right panel in Fig. 2. The fiducial episode masses are 10.4, 19.7, 101.9, and 348.0 $M_\odot$, while the upper branch gives 34.6, 65.6, 339.5, and 599.9 $M_\odot$. Summed over the full sequence, the cumulative mass lost reaches $4.80 \times 10^2\,M_\odot$ on the fiducial branch and $1.04 \times 10^3\,M_\odot$ on the upper branch. Even the larger of these remains at only the $\sim 1\%$ level of the $\sim 10^5\,M_\odot$ star. The pulsations therefore do not disrupt the SMS as a whole. They remove a modest but physically important fraction of the outer envelope. The final episode dominates this budget, contributing $\simeq 73\%$ of the cumulative fiducial loss and $\simeq 58\%$ of the cumulative upper-limit loss.

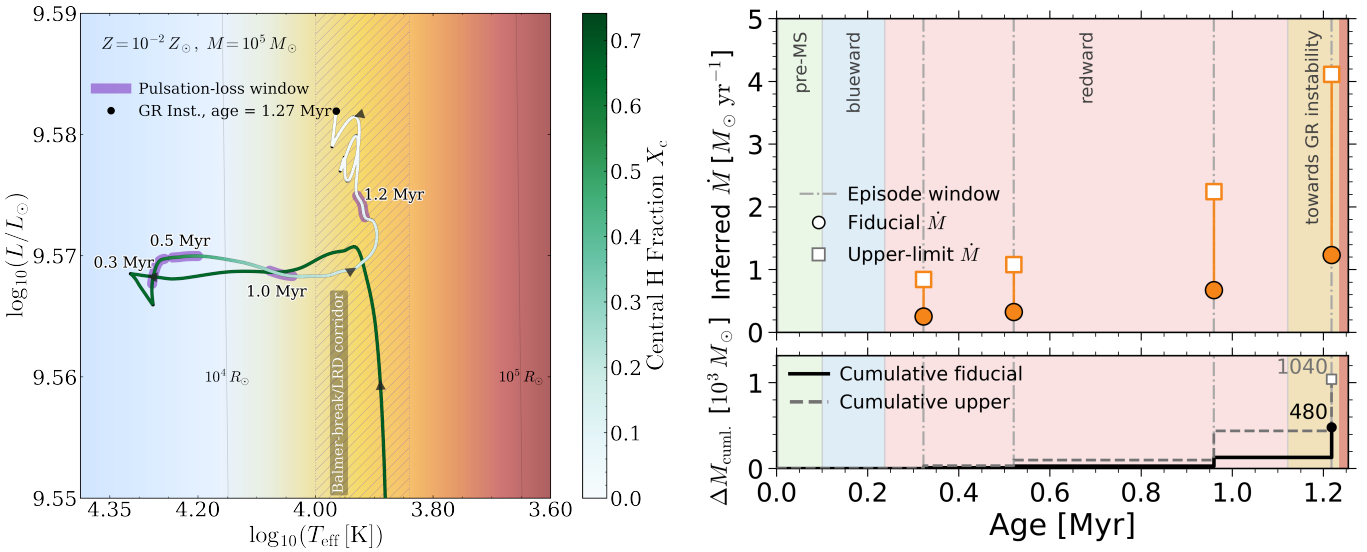

Figure 2. *Left:* Post-accretion Hertzsprung–Russell evolution of the $10^5\,M_\odot$, $Z = 10^{-2}\,Z_\odot$ model commences at $\log(L/L_\odot) = 9.57$, $\log T_{\rm eff} = 3.90$. The track is colored by the central hydrogen mass fraction, $X_{\rm c}$. Purple segments mark phases with pulsation-driven mass loss, the black circle marks the onset of GR instability, and the hatched band indicates the Balmer-break/LRD corridor. Thin black curves show lines of constant radius. *Right:* Pulsation-driven mass-loss history of the same sequence. The top panel shows the episode-averaged mass-loss rate for the fiducial and upper branches, and the bottom panel shows the cumulative ejected mass. Four discrete episodes occur at 0.322, 0.520, 0.959, and 1.218 Myr, with both the rates and integrated ejecta increasing toward late times. The final pre-collapse episode dominates the total mass lost.

The physical trend is equally clear. All four active episodes are classified as strange-mode dominated in our channel decomposition, consistent with strongly nonadiabatic, surface-centered driving in the radiation-dominated envelope. The first two events remain modest. The third is already an order of magnitude stronger in ejected mass than the first, and the fourth becomes the defining mass-loss event of the sequence. This strengthening is not caused by a steadily growing reservoir, since the accessible mass cap stays near $6\times10^2\,M_\odot$ across all four episodes. A more natural interpretation is that, as the star returns to an extended cool configuration and approaches both the Balmer-break corridor and the onset of GR instability, the coupling between the pulsation and the outer envelope becomes markedly more effective.

3.3. *Event durations and launch conditions*

The two panels of Fig. 3 place the four mass-loss episodes on complementary physical scales. In the left panel, the effective durations ($\Delta t_{\rm eff}$) are 41.1, 60.6, 151.2, and 281.9 yr for episodes 1–4. These values are far longer than the linear pulsation periods (P), 0.411, 0.606, 1.512, and 2.819 yr, and also longer than the corresponding growth e-folding times ($\tau_{\rm grow}$), 0.412, 0.406, 0.688, and 2.242 yr. Each event therefore lasts for $\sim 100P$, or roughly 10^2 to 2×10^2 growth times. At the same time, the events remain far shorter than the local evolutionary half-gaps, which are 9.9×10^4, 8.8×10^4, 7.0×10^4, and 6.0×10^4 yr. They are therefore neither single-cycle impulses nor quasi-steady winds, but intrinsically finite pulsation episodes.

The right panel shows how the launch conditions evolve from one episode to the next. The structural escape speed declines from 2587 and 2283 km s^{-1} in the first two episodes to 1583 and 1176 km s^{-1} in the third and fourth. Over the same interval, the linear pulsation speed scale R/P remains much smaller, falling only from 307 to 216 km s^{-1}. Taken on its own, that scale is too small to unbind the outer layers. The sinusoidal scale $2\pi R/P$, however, rises to a large fraction of the escape speed in the first three events, with $v_{2\pi R/P}/v_{\rm esc} \simeq 0.74$, 0.73, and 0.88, and reaches 1.15 in the final episode. By the last event, the natural pulsation speed scale has therefore become comparable to, and slightly larger than, the local escape threshold.

The two radiative reference scales in Fig. **??** separate a momentum constraint from an energy constraint. The lower radiative point is the single-scattering momentum scale, $v_{L/c} = L_\star/(\dot{M}c)$. Because these events are discrete pulsation-driven ejections rather than steady winds, we use $v_{L/c}$ only as a benchmark for whether a purely radiative, momentum-limited outflow could launch the inferred event-averaged mass flux. On the fiducial branch, $v_{L/c}$ decreases from 298 and 232 km s^{-1} in the first two episodes to 111 and 61.5 km s^{-1} in the third and fourth, and remains well below $v_{\rm esc}$ through-

out. The upper radiative point is the photon-tiring scale, which instead remains comfortably above escape in all four cases, ranging from 1.31×10^4 to 5.96×10^3 km s^{-1}. The global radiative energy budget is therefore sufficient, but a purely momentum-limited radiative outflow would still struggle on its own. The limiting factor is how efficiently strange-mode pulsations couple that available energy to the weakly bound outer envelope.

Taken together, Fig. 3 shows why the final outburst dominates the sequence. It is the longest-lived event, it occurs when the envelope is least tightly bound, and it is the only episode for which $2\pi R/P$ overtakes $v_{\rm esc}$. The key result is therefore clear: the luminosity can power the ejection, but only the late strange-mode pulsations couple that energy efficiently enough to launch the outer envelope. As shown in Sec. 3.4 and discussed further in Sec. 4.2, this also makes the final shell the only one likely to remain optically relevant during an LRD-like phase: the earlier ejecta expand and dilute, whereas the last event can still form a compact reprocessing layer on timescales of only a few to a few tens of years.

3.4. *Circumstellar outcome at near the onset of collapse*

Figure 4 maps the four strange-mode mass-loss episodes into the circumstellar structural parameters present at the end of the model. The launch-speed brackets, inferred from Fig. 3, vary only modestly from one episode to the next, with $v_{\rm low} \simeq 0.22$–0.31×10^3 km s^{-1} and $v_{\rm high} \simeq 1.36$–1.93×10^3 km s^{-1}. The circumstellar outcome is therefore shaped less by a large change in launch speed than by a large difference in coasting time: the first three eruptions have had hundreds of thousands of years to travel outward, whereas the fourth is created only shortly before collapse.

This contrast is clear in the right panel of Fig. 4. By the onset of collapse, the first three fiducial episodes occupy shell-like bands with inner radii of 281.0, 190.4, and 59.0 pc and outer radii of 1765.5, 1196.3, and 370.6 pc. The fourth event is qualitatively different. Its inner edge remains at the stellar radius, 6.23×10^{-4} pc, and its outer edge reaches only 0.392 pc. The result is a strongly stratified circumstellar structure: three old, highly extended shells surround a single compact inner ejection that remains close to the star.

The optical-depth contrast is equally sharp. For the first three episodes, the geometric optical depths are negligible, $\tau_{\rm geo} \simeq 1.18 \times 10^{-10}$, 4.89×10^{-10}, and 2.63×10^{-8}, and even the corresponding inner-edge values remain tiny, at 7.42×10^{-10}, 3.07×10^{-9}, and 1.66×10^{-7}. The fourth shell again stands apart: $\tau_{\rm geo} \simeq 8.04$, $\tau_{\rm in} \simeq 5.06 \times 10^3$, and $\tau_{\rm out} \simeq 1.28 \times 10^{-2}$. Within this approximation, only the last event can provide an optically important circumstellar shell at collapse. These values are order-of-magnitude diagnostics based on a constant opacity, $\kappa = 0.34\,{\rm cm^2\,g^{-1}}$, rather than full radiative-transfer solutions. A conceptually similar behavior is observed in R Coronae Borealis-type variable stars, F-to-G type hydrogen-deficient supergiants, which experience episodic fading of their optical brightness by a factor of up-to 5000 explained by the ejection of optically thick dusty shells (see e.g., I. Iben et al. 1996).

Finally, the shell masses reinforce the same picture. On the fiducial branch, the first three events eject 10.4, 19.7, and 101.9 $M_\odot$, while the final episode contributes 348.0 $M_\odot$. By collapse, the first three strange-mode eruptions have diluted into very extended, optically negligible relics, whereas the final event remains both compact and massive enough to set the immediate circumstellar environment.

3.5. *Composition of the final ejecta*

Since Fig. 4 shows that the immediate pre-collapse environment is set by the fourth and final eruption, we now examine the composition of that shell in Fig. 5. The left panel shows the abundance profile at $t = 1.218$ Myr together with the fiducial and upper ejection windows. Both sample the outer radiative envelope and remain overwhelmingly H/He rich. The upper window reaches slightly deeper, but the overall CNO pattern remains similar in the two cases.

The right panel of Fig. 5 shows the integrated shell masses. In the fiducial shell, the ejecta contain 243 $M_\odot$ of H and 105 $M_\odot$ of He, together with 4.84×10^{-3}, 1.3×10^{-2}, and 1.1×10^{-2} $M_\odot$ in C, N, and O. The upper shell follows the same pattern, with 419 $M_\odot$ of H, 180 $M_\odot$ of He, and 8.35×10^{-3}, 2.24×10^{-2}, and 2.04×10^{-2} $M_\odot$ in C, N, and O. In both cases the shell is therefore H/He dominated by mass, while the trace heavy-element pattern is nitrogen rich, with $N > O > C$.

The logarithmic number ratios make the same point more clearly. For the fiducial shell we obtain $\log(N/O) \simeq 0.13$ and $\log(C/O) \simeq -0.23$. For the upper shell the corresponding values are $\log(N/O) \simeq 0.10$ and $\log(C/O) \simeq -0.26$. The He/H number ratio is also nearly unchanged, with He/H $\simeq 0.108$ and 0.107 for the fiducial and upper shells. The key result is that the nitrogen excess is robust. It survives the uncertainty in how deeply the final eruption reaches into the outer envelope.

This is the main message of Fig. 5. The final strange-mode shell is not merely H rich. It carries a distinctive

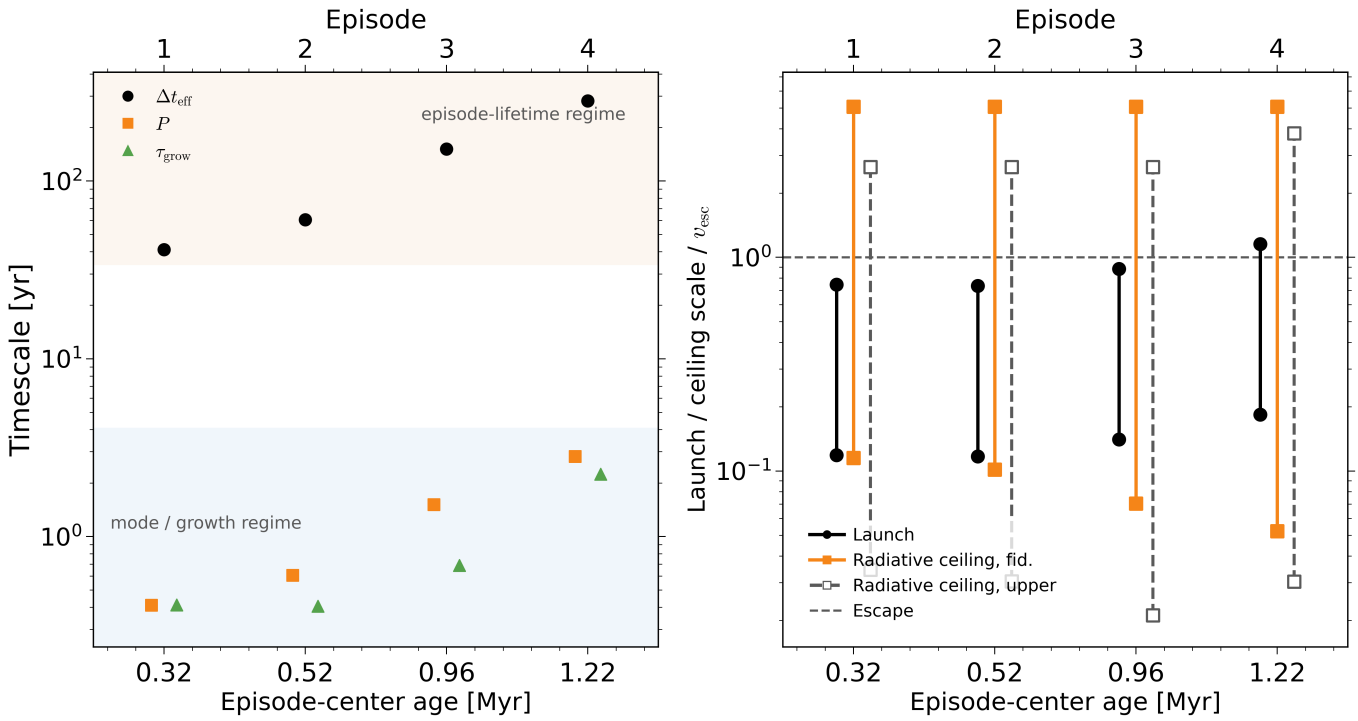

Figure 3. Timescale and velocity diagnostics for the four pulsation-driven mass-loss episodes in the $Z = 10^{-2}\,Z_\odot$ $10^5\,M_\odot$ sequence. *Left:* effective episode durations compared with the mode period, the linear growth e-folding time, and the local half-gap between adjacent stored models. The events last 41.1, 60.6, 151.2, and 281.9 yr, corresponding to ~ 100 pulsation cycles in each case, and remain far shorter than the local evolutionary spacing. *Right:* structural escape speed, characteristic pulsation speeds R/P and $2\pi R/P$, and two radiative reference scales on the fiducial branch: the lower point gives the single-scattering momentum scale $v_{L/c}$, while the upper point gives the photon-tiring scale $v_{\rm tir}$.

chemical signature. In our earlier SMS calculations, enhanced N/O emerged as a recurring abundance fingerprint of SMS ejecta (D. Nandal et al. 2024a,c, 2025b,c). The shell shown here therefore provides an explicit composition prediction for the compact circumstellar material present at collapse, with direct observational diagnostics in N/O, C/O, and He/H.

Taken together, these results define a late-time SMS mass-loss channel in which rare strange-mode outbursts eject only a modest fraction of the envelope, while the final pre-collapse event leaves behind the compact, chemically distinctive shell most relevant to the LRD phase.

4. DISCUSSION

4.1. *From SMS to a Direct Collapse Black Hole*

The final fate of the $Z = 10^{-2}\,Z_\odot$ SMS is set by general-relativistic instability. We compute three estimates of the onset of the GR radial instability based on individual stellar snapshots. A linear adiabatic GR criterion of H. Saio et al. (2024) and post-Newtonian estimate of L. Haemmerlé (2021b) both place the onset of instability at an age of roughly 1.3 Myr, while a relativistic adiabatic analysis which accounts for non-linear perturbations finds a slightly earlier onset at 0.9 Myr (C. Nagele et al. 2022). The 1D GR hydrodynamics follow-up confirms that this earlier model collapses to a black hole. All three criteria agree that the SMS will live for approximately one mega-year and will form a black hole after losing a small fraction of its envelope. The GR hydrodynamics calculation shows that this black hole will form within roughly 10^4 s of the instability, and that the vast majority of the stellar material will fall into the black hole. In this sense, the SMS provides a direct pathway to a $\sim 10^5\,M_\odot$ direct-collapse black hole.

We caveat that we have not included all relevant forms of mass loss in these calculations, and therefore may be underestimating the amount of mass ejected. In particular, line driven winds (C. Nagele & H. Umeda 2023; C. Nagele et al. 2023a) and thermonuclear driven pulsations (C. Nagele et al. 2022, 2023b; C. Nagele & H. Umeda 2024) can both liberate $100 \sim 1000\,M_\odot$ of SMS material. The more material ejected, the lighter the remnant black hole, but also the longer the cocoon remains optically thick and resembles an LRD. For instance if strange mode ejecta remains marginally bound, or is decelerated by the dense natal reservoir and stalls at the shell scale of 0.392 pc, that ejecta would return on a fallback timescale of $\sim 1.3 \times 10^4$ yr. Larger ejecta

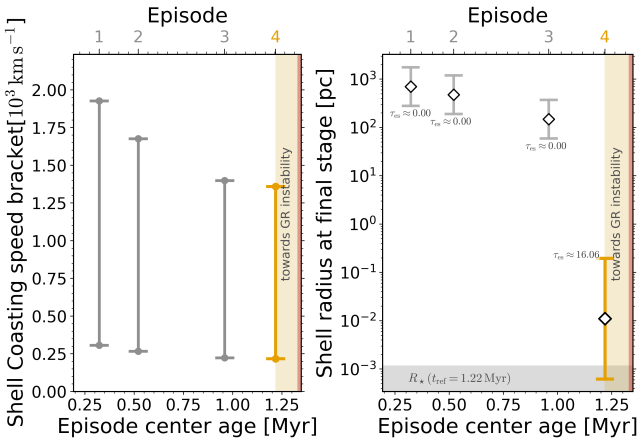

Figure 4. Shell morphology implied by the four pulsation–driven mass-loss episodes at the end of the $Z = 10^{-2}\,Z_\odot$ $10^5\,M_\odot$ model. The reference epoch is the end of the fourth episode. The first three ejections have already coasted to large radii and are optically thin, with shell bands spanning $\sim$ 59 to 1766 pc and negligible optical depth. The fourth event remains compact, extending from the stellar radius to only 0.392 pc, and is the only shell that remains optically important at collapse, with $\tau_{\rm geo} \simeq 8$. The immediate circumstellar environment is therefore set by the final strange-mode eruption, while the earlier episodes survive only as diffuse outer relics.

masses and stall radii would lead to longer fall-back times. The importance of this fallback mechanism is to prolong the lifetime of the optically thick cocoon and to provide a new reservoir for accretion: if the returning gas retains sufficient angular momentum, part of it could circularize into a disc, providing a possible link between SMS collapse and a longer-lived, gas-enshrouded accreting source (M. C. Begelman et al. 2008; R. P. Naidu et al. 2025).

4.2. *Pulsation-driven shells as the origin of cool LRD continua*

Some recent works have argued that at least part of the LRD continuum arises from cool dense gas with characteristic temperatures of a few 10^3 K (H. Liu et al. 2025; D. Kido et al. 2025; B. Wang et al. 2026; A. de Graaff et al. 2025b). Our models offer a natural way to produce such values. The low observed temperature does not have to trace the hydrostatic SMS surface. It can instead be set by the last optically thick shell ejected by pulsations.

The shell properties in our $Z = 10^{-2}\,Z_\odot$ model are already sufficient for this. The luminosity stays near $\log(L/L_\odot) \simeq 9.57$. Re-emitting that luminosity at 4000 K requires a photospheric radius of only $\simeq 5.9 \times 10^2$ AU. For 3000 K, the required radius is $\simeq 1.05 \times 10^3$ AU. These radii are only a few times larger than the hydrostatic SMS radius for $T_{\rm eff} \sim 7000$–8000 K, and they remain far inside the final shell extent of ~ 0.392 pc.

The onset timescale is also short. Using the launch-speed range of the last ejection, $v \simeq 2.2 \times 10^2$–1.36×10^3 km s^{-1}, the shell reaches the 4000 K radius in only $\sim$ 2–13 yr. It reaches the 3000 K radius in only $\sim$ 4–23 yr. A cool apparent photosphere can therefore be established within only a few years to a few tens of years after ejection. The inferred shell mass, $\sim 3.5 \times 10^2$–$6 \times 10^2\,M_\odot$, is large enough that only a modest continuum opacity is required for part of the ejecta to maintain $\tau \sim 1$ at these radii. Adiabatic expansion and later dust formation would strengthen the same trend. In this picture, an intrinsically hotter SMS can still produce a continuum with an apparent temperature of only 3000–4000 K.

4.3. *Predicted observational signatures*

The predicted photospheric $T_{\rm eff} \sim 7000$ K and dusty shells should give the SMS a yellow-hypergiant-like appearance. This is a rare stellar class in the Milky Way and nearby galaxies, but scaled up in luminosity and with a different abundance pattern. Objects such as *IRC+10420* and *IRAS 17163-3907* (the "Fried Egg Nebula") show moderately reddened late-A/early-F spectra with characteristic (broad) emission and absorption lines formed in their complex circumstellar envelopes (R. M. Humphreys et al. 1997, 2002; E. Lagadec et al. 2011; S. H. J. Wallström et al. 2015). SMSs should generate such features, although the different fiducial layer abundance pattern shown in Fig. 5 can modify various absorption-line ratios. We may expect weaker oxygen, carbon, and magnesium, and stronger nitrogen features. Any iron lines would reflect the composition of the birth gas rather than in-situ production during the hydrogen-burning stage.

Pulsation-driven mass loss produces multiple shell components with characteristic launch speeds of order 10^2–10^3 km s^{-1}. This should produce blueshifted multi-component absorption lines, or asymmetric profiles if the components blend, from atomic species such as Na I and K I at sufficiently high column density. At the same time, line-driven mass loss at $10^{-2}\,Z_\odot$ should produce more classical wind signatures, including P Cygni-like profiles in lines such as Hα and metastable He I. Such broad hydrogen and helium features are already seen in LRDs at both low (R. Lin et al. 2025; X. Ji et al. 2026) and high redshift (J. Matthee et al. 2026).

5. CONCLUSION

In this Letter, we asked whether late pulsational mass loss from supermassive stars can assemble the compact

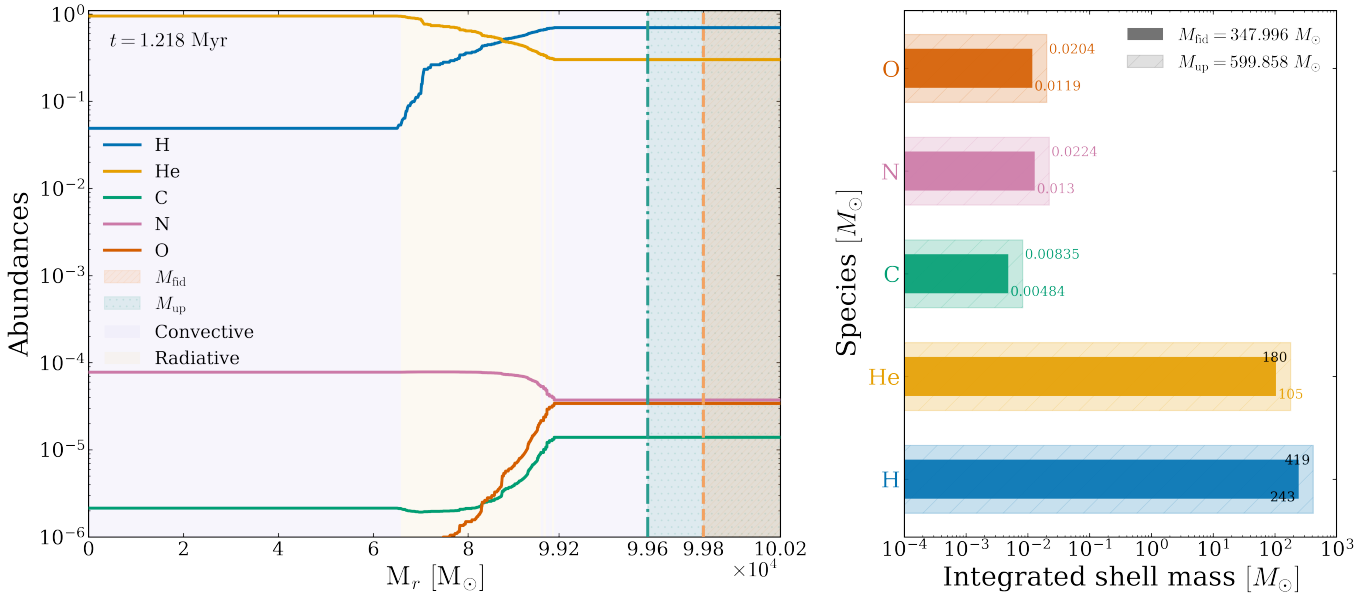

Figure 5. Composition of the final pulsation-driven shell at $t = 1.218$ Myr. The *left panel* shows the abundance profile of the outer envelope together with the fiducial and upper ejection windows; both sample the outer radiative layers, with the upper window reaching slightly deeper. The *right panel* shows the integrated shell masses of H, He, C, N, and O for the fiducial and upper shells. In both cases the ejecta are dominated by H and He, but the trace CNO composition is nitrogen rich.

circumstellar material required in SMS-based interpretations of LRDs. Our results show that it can. Late strange-mode pulsations create a small number of discrete pre-collapse ejection episodes that build a compact inner shell without removing more than a modest fraction of the stellar mass. Across the full metallicity range from Pop III to $10^{-2}\,Z_\odot$, this shell-ejection channel persists.

- **Late-time SMS mass loss by pulsations is discrete rather than steady.** The mass loss does not appear as a persistent wind phase. It is concentrated into a finite number of strange-mode ejection episodes, separated by long intervals of relative quiescence. In the $Z = 10^{-2}\,Z_\odot$ model, which provides the clearest LRD analogue, only four fiducial episodes occur. They last 41.1, 60.6, 151.2, and 281.9 yr, and eject 10.4, 19.7, 101.9, and 348.0 $M_\odot$.

- **The shell relevant to the LRD phase is set by the last major ejection.** Earlier ejecta have hundreds of thousands of years to coast outward and become optically negligible. The final pre-collapse event remains compact, extending only from the stellar radius to ~ 0.392 pc, and is the only shell that remains optically important at collapse, with $\tau_{\rm geo} \simeq 8$. The observationally relevant shell is therefore not the accumulated residue of prior mass loss. It is the direct product of the final strange-mode outburst.

- **The final shell comes with direct, testable predictions.** In the fiducial $Z = 10^{-2}\,Z_\odot$ case, the final shell contains $\sim 243\,M_\odot$ of H and $\sim 105\,M_\odot$ of He, together with a robust nitrogen-rich trace composition, $\log(N/O) \simeq 0.13$ and $\log(C/O) \simeq -0.23$. The ejecta are launched with characteristic speeds of order 10^2–10^3 km s^{-1}. The shell therefore carries quantitative predictions in mass, radius, velocity, and composition that can be confronted directly with LRD observations.

- **Pulsations reshape the surroundings without erasing the heavy seed.** In the $Z = 10^{-2}\,Z_\odot$ model, the total ejected mass is only $4.80 \times 10^2\,M_\odot$ on the fiducial branch and $1.04 \times 10^3\,M_\odot$ on the upper branch, remaining a small fraction of the stellar mass. The star reaches GR instability at an age of ~ 1 Myr, and collapses on a timescale of 10^4 s. The resulting seed therefore remains close to the stellar mass at instability, of order $10^5\,M_\odot$.

These results place SMSs at the center of several ideas that are often discussed separately. In the direct-collapse picture, massive black-hole seeds form directly from collapsing protogalactic gas. In quasi-star models,

a black hole grows inside a massive hydrostatic envelope. In recent BH⋆ interpretations of LRDs, a black hole is embedded in dense gas that shapes the emergent spectrum (R. Barkana & A. Loeb 2004; M. C. Begelman et al. 2008; R. P. Naidu et al. 2025). Our results suggest that SMS evolution can provide the bridge between these frameworks: it can first assemble the compact shell required for the observable LRD phase, and then collapse almost intact into the heavy seed itself. In this sense, the SMS links the circumstellar structure, the LRD appearance, and the birth of the massive black-hole seed in one continuous evolutionary pathway.

A logical next step is to turn these shell properties into forward models of continua and line diagnostics, so that pulsational shell ejection from SMSs can be tested directly against the observed spectra of LRDs.

ACKNOWLEDGMENTS

DN was supported by the Swiss National Science Fund (SNSF) Postdoctoral Fellowship, grant number: P500-2235464. DN would like to thank Prof. Hideyuki Saio for his foundational work and for his support during the early stages of this project. FEB acknowledges support from ANID-Chile BASAL CATA FB210003 and FONDECYT Regular 1241005. Artificial intelligence tools were used during manuscript preparation for spell-checking and formatting assistance.

REFERENCES

Akins, H. B., Casey, C. M., Lambrides, E., et al. 2025, *Astrophys. J.*, 991, 37, doi: 10.3847/1538-4357/ade984

Appenzeller, I., & Fricke, K. 1972, *Astro. Astrophys.*, 21, 285

Asada, Y., Inayoshi, K., Fei, Q., Fujimoto, S., & Willott, C. 2026, arXiv e-prints, arXiv:2601.10573, doi: 10.48550/arXiv.2601.10573

Baggen, J. F. W., van Dokkum, P., Brammer, G., et al. 2024, *Astrophys. J.*, 977, L13, doi: 10.3847/2041-8213/ad90b8

Barkana, R., & Loeb, A. 2004, *Astrophys. J.*, 609, 474, doi: 10.1086/421079

Begelman, M. C., Rossi, E. M., & Armitage, P. J. 2008, *Mon. Not. Royal Astron. Soc.*, 387, 1649, doi: 10.1111/j.1365-2966.2008.13344.x

Begelman, M. C., Volonteri, M., & Rees, M. J. 2006, *Mon. Not. Royal Astron. Soc.*, 370, 289, doi: 10.1111/j.1365-2966.2006.10467.x

Bromm, V., & Loeb, A. 2003, *Astrophys. J.*, 596, 34, doi: 10.1086/377529

Chandrasekhar, S. 1964, *Astrophys. J.*, 140, 417, doi: 10.1086/147938

Chisholm, J., Berg, D. A., Boylan-Kolchin, M., et al. 2026, arXiv e-prints, arXiv:2602.15935, doi: 10.48550/arXiv.2602.15935

de Graaff, A., Rix, H.-W., Naidu, R. P., et al. 2025a, *Astro. Astrophys.*, 701, A168, doi: 10.1051/0004-6361/202554681

de Graaff, A., Hviding, R. E., Naidu, R. P., et al. 2025b, arXiv e-prints, arXiv:2511.21820, doi: 10.48550/arXiv.2511.21820

de Jager, C., Nieuwenhuijzen, H., & van der Hucht, K. A. 1988, *Astro. Astrophys. Suppl.*, 72, 259

Fowler, W. A. 1966, *Astrophys. J.*, 144, 180, doi: 10.1086/148594

Fuller, G. M., Woosley, S. E., & Weaver, T. A. 1986, *Astrophys. J.*, 307, 675, doi: 10.1086/164452

Furtak, L. J., Zitrin, A., Plat, A., et al. 2023, *Astrophys. J.*, 952, 142, doi: 10.3847/1538-4357/acdc9d

Glatzel, W. 1994, *Mon. Not. Royal Astron. Soc.*, 271, 66, doi: 10.1093/mnras/271.1.66

Godart, M., Dupret, M.-A., Noels, A., et al. 2011, in IAU Symposium, Vol. 272, Active OB Stars: Structure, Evolution, Mass Loss, and Critical Limits, ed. C. Neiner, G. Wade, G. Meynet, & G. Peters, 503–504, doi: 10.1017/S1743921311011185

Guhathakurta, P., Grion Filho, D., Bhattacharya, A. R., et al. 2025, *Astrophys. J.*, 987, 203, doi: 10.3847/1538-4357/adcc2c

Haemmerlé, L. 2021a, *Astro. Astrophys.*, 647, A83, doi: 10.1051/0004-6361/202039686

Haemmerlé, L. 2021b, *Astro. Astrophys.*, 650, A204, doi: 10.1051/0004-6361/202140893

Haemmerlé, L., Woods, T. E., Klessen, R. S., Heger, A., & Whalen, D. J. 2018, *Mon. Not. Royal Astron. Soc.*, 474, 2757, doi: 10.1093/mnras/stx2919

Harikane, Y., Zhang, Y., Nakajima, K., et al. 2023, *Astrophys. J.*, 959, 39, doi: 10.3847/1538-4357/ad029e

Hosokawa, T., Omukai, K., & Yorke, H. W. 2012a, *Astrophys. J.*, 756, 93, doi: 10.1088/0004-637X/756/1/93

Hosokawa, T., Yoshida, N., Omukai, K., & Yorke, H. W. 2012b, *Astrophys. J.*, 760, L37, doi: 10.1088/2041-8205/760/2/L37

Hoyle, F., & Fowler, W. A. 1963, *Mon. Not. Royal Astron. Soc.*, 125, 169

Humphreys, R. M., Davidson, K., & Smith, N. 2002, *Astron. J.*, 124, 1026, doi: 10.1086/341380

Humphreys, R. M., Smith, N., Davidson, K., et al. 1997, *Astron. J.*, 114, 2778, doi: 10.1086/118686

Iben, Jr., I., Tutukov, A. e. V., & Yungelson, L. R. 1996, *Astrophys. J.*, 456, 750, doi: 10.1086/176694

Inayoshi, K., Hosokawa, T., & Omukai, K. 2013, *Mon. Not. Royal Astron. Soc.*, 431, 3036, doi: 10.1093/mnras/stt362

Inayoshi, K., & Maiolino, R. 2025, *Astrophys. J.*, 980, L27, doi: 10.3847/2041-8213/adaebd

Ji, X., Maiolino, R., Übler, H., et al. 2025, *Mon. Not. Royal Astron. Soc.*, 544, 3900, doi: 10.1093/mnras/staf1867

Ji, X., D'Eugenio, F., Juodžbalis, I., et al. 2026, *Mon. Not. Royal Astron. Soc.*, 545, staf2235, doi: 10.1093/mnras/staf2235

Kido, D., Ioka, K., Hotokezaka, K., Inayoshi, K., & Irwin, C. M. 2025, *Mon. Not. Royal Astron. Soc.*, 544, 3407, doi: 10.1093/mnras/staf1898

Kiriakidis, M., Fricke, K. J., & Glatzel, W. 1993, *Mon. Not. Royal Astron. Soc.*, 264, 50, doi: 10.1093/mnras/264.1.50

Kocevski, D. D., Finkelstein, S. L., Barro, G., et al. 2025, *Astrophys. J.*, 986, 126, doi: 10.3847/1538-4357/adbc7d

Kokorev, V., Chisholm, J., Naidu, R. P., et al. 2025, arXiv e-prints, arXiv:2511.07515, doi: 10.48550/arXiv.2511.07515

Lagadec, E., Zijlstra, A. A., Oudmaijer, R. D., et al. 2011, *Astro. Astrophys.*, 534, L10, doi: 10.1051/0004-6361/201117521

Levesque, E. M. 2017, Astrophysics of Red Supergiants (Institute of Physics), doi: 10.1088/978-0-7503-1329-2

Lin, R., Zheng, Z.-Y., Jiang, C., et al. 2025, *Astrophys. J.*, 980, L34, doi: 10.3847/2041-8213/adaaf1

Liu, H., Jiang, Y.-F., Quataert, E., Greene, J. E., & Ma, Y. 2025, *Astrophys. J.*, 994, 113, doi: 10.3847/1538-4357/ae0c19

Maeder, A., & Meynet, G. 2000, *Astro. Astrophys.*, 361, 159, doi: 10.48550/arXiv.astro-ph/0006405

Maiolino, R., Uebler, H., D'Eugenio, F., et al. 2025, arXiv e-prints, arXiv:2505.22567, doi: 10.48550/arXiv.2505.22567

Matthee, J., Naidu, R. P., Brammer, G., et al. 2024, *Astrophys. J.*, 963, 129, doi: 10.3847/1538-4357/ad2345

Matthee, J., Torralba, A., Pezzulli, G., et al. 2026, arXiv e-prints, arXiv:2603.17667, doi: 10.48550/arXiv.2603.17667

Nagele, C., & Umeda, H. 2023, *Astrophys. J.*, 949, L16, doi: 10.3847/2041-8213/acd550

Nagele, C., & Umeda, H. 2024, Phys. Rev. D, 110, L061301, doi: 10.1103/PhysRevD.110.L061301

Nagele, C., Umeda, H., & Takahashi, K. 2023a, *Mon. Not. Royal Astron. Soc.*, 523, 1629, doi: 10.1093/mnras/stad1522

Nagele, C., Umeda, H., Takahashi, K., & Maeda, K. 2023b, *Mon. Not. Royal Astron. Soc.*, 520, L72, doi: 10.1093/mnrasl/slad009

Nagele, C., Umeda, H., Takahashi, K., Yoshida, T., & Sumiyoshi, K. 2020, *Mon. Not. Royal Astron. Soc.*, 496, 1224, doi: 10.1093/mnras/staa1636

Nagele, C., Umeda, H., Takahashi, K., Yoshida, T., & Sumiyoshi, K. 2021, *Mon. Not. Royal Astron. Soc.*, 508, 828, doi: 10.1093/mnras/stab2592

Nagele, C., Umeda, H., Takahashi, K., Yoshida, T., & Sumiyoshi, K. 2022, *Mon. Not. Royal Astron. Soc.*, 517, 1584, doi: 10.1093/mnras/stac2495

Naidu, R. P., Matthee, J., Katz, H., et al. 2025, arXiv e-prints, arXiv:2503.16596, doi: 10.48550/arXiv.2503.16596

Nakauchi, D., Inayoshi, K., & Omukai, K. 2020, *Astrophys. J.*, 902, 81, doi: 10.3847/1538-4357/abb463

Nandal, D., Buldgen, G., Whalen, D. J., et al. 2025a, arXiv e-prints, arXiv:2506.08268, doi: 10.48550/arXiv.2506.08268

Nandal, D., Buldgen, G., Whalen, D. J., et al. 2025b, *Astro. Astrophys.*, 701, A262, doi: 10.1051/0004-6361/202555878

Nandal, D., & Chon, S. 2026, *Astrophys. J.*, 999, 110, doi: 10.3847/1538-4357/ae40bb

Nandal, D., Farrell, E., Buldgen, G., Meynet, G., & Ekström, S. 2024a, *Astro. Astrophys.*, 685, A159, doi: 10.1051/0004-6361/202345997

Nandal, D., & Loeb, A. 2026, *Astrophys. J.*, 998, 124, doi: 10.3847/1538-4357/ae32f3

Nandal, D., Regan, J. A., Woods, T. E., et al. 2023, *Astro. Astrophys.*, 677, A155, doi: 10.1051/0004-6361/202346938

Nandal, D., Regan, J. A., Woods, T. E., et al. 2024b, *Astro. Astrophys.*, 683, A156, doi: 10.1051/0004-6361/202348035

Nandal, D., Sibony, Y., & Tsiatsiou, S. 2024c, *Astro. Astrophys.*, 688, A142, doi: 10.1051/0004-6361/202348866

Nandal, D., Whalen, D. J., Latif, M. A., & Heger, A. 2025c, *Astrophys. J.*, 994, L11, doi: 10.3847/2041-8213/ae1a63

Regan, J. A., Wise, J. H., O'Shea, B. W., & Norman, M. L. 2020, *Mon. Not. Royal Astron. Soc.*, 492, 3021, doi: 10.1093/mnras/staa035

Reinoso, B., Klessen, R. S., Schleicher, D., Glover, S. C. O., & Solar, P. 2023, *Mon. Not. Royal Astron. Soc.*, 521, 3553, doi: 10.1093/mnras/stad790

Rusakov, V., Watson, D., Nikopoulos, G. P., et al. 2026, *Nature*, 649, 574, doi: 10.1038/s41586-025-09900-4

Saio, H., Baker, N. H., & Gautschy, A. 1998, *Mon. Not. Royal Astron. Soc.*, 294, 622, doi: 10.1111/j.1365-8711.1998.01195.x10.1046/j.1365-8711.1998.01195.x

Saio, H., Georgy, C., & Meynet, G. 2013, in Astronomical Society of the Pacific Conference Series, Vol. 479, Progress in Physics of the Sun and Stars: A New Era in Helio- and Asteroseismology, ed. H. Shibahashi & A. E. Lynas-Gray, 47, doi: 10.48550/arXiv.1305.4728

Saio, H., Nandal, D., Ekström, S., & Meynet, G. 2024, *Astro. Astrophys.*, 689, A169, doi: 10.1051/0004-6361/202449971

Sakurai, Y., Hosokawa, T., Yoshida, N., & Yorke, H. W. 2015, *Mon. Not. Royal Astron. Soc.*, 452, 755, doi: 10.1093/mnras/stv1346

Setton, D. J., Greene, J. E., de Graaff, A., et al. 2025, *Astrophys. J.*, 995, 118, doi: 10.3847/1538-4357/ae1500

Sonoi, T., & Shibahashi, H. 2014, PASJ, 66, 69, doi: 10.1093/pasj/psu045

Vink, J. S., de Koter, A., & Lamers, H. J. G. L. M. 2001, *Astro. Astrophys.*, 369, 574, doi: 10.1051/0004-6361:20010127

Wallström, S. H. J., Muller, S., Lagadec, E., et al. 2015, *Astro. Astrophys.*, 574, A139, doi: 10.1051/0004-6361/201321516

Wang, B., Leja, J., Labbe, I., et al. 2026, arXiv e-prints, arXiv:2602.06024, doi: 10.48550/arXiv.2602.06024

Wise, J. H., Regan, J. A., O'Shea, B. W., et al. 2019, *Nature*, 566, 85, doi: 10.1038/s41586-019-0873-4

Woods, T. E., Heger, A., & Haemmerlé, L. 2020, *Mon. Not. Royal Astron. Soc.*, 494, 2236, doi: 10.1093/mnras/staa763

Woods, T. E., Heger, A., Whalen, D. J., Haemmerlé, L., & Klessen, R. S. 2017, *Astrophys. J.*, 842, L6, doi: 10.3847/2041-8213/aa7412

Yadav, A. P., Kühnrich Biavatti, S. H., & Glatzel, W. 2018, *Mon. Not. Royal Astron. Soc.*, 475, 4881, doi: 10.1093/mnras/sty092

Zwick, L., Tiede, C., & Mayer, L. 2025, arXiv e-prints, arXiv:2507.22014, doi: 10.48550/arXiv.2507.22014

APPENDIX

A. EXTENDED METHODS

We analyse the full evolutionary outputs of five GENEC supermassive-star sequences. Each stored model is treated as a complete stellar structure at one evolutionary time: we read the full radial profile from the `StrucData` file and use the auxiliary `v` file, when present, to supply additional thermodynamic and transport quantities. The calculation is therefore performed on the full star for every stored model, rather than on a reduced envelope subset.

For each model we retain the radial profiles needed for the pulsation analysis,

$$r, \quad M_r, \quad P, \quad \rho, \quad T, \quad \kappa, \quad \epsilon, \quad L_{\rm rad}, \quad L_{\rm tot},$$

together with composition, convective quantities, and the thermodynamic derivatives used to evaluate the adiabatic exponents,

$$\Gamma_1 = \frac{\chi_\rho}{1-\chi_T\nabla_{\rm ad}}, \tag{A1}$$

$$\Gamma_3 - 1 = \Gamma_1\nabla_{\rm ad}. \tag{A2}$$

Before proceeding, we require the structure to remain physically well behaved, including monotonic radius and enclosed mass and finite thermodynamic variables.

A.1. *Candidate envelope regions*

The later nonadiabatic analysis is not carried out blindly over the whole star. Instead, we first identify physically motivated envelope regions where radial driving is most likely to occur. These include the H, He I, and He II partial-ionization zones, the iron-opacity bump, the deeper iron feature, and a near-surface radiative layer (H. Saio et al. 2024). In practice we use the temperature intervals

$$\text{H}: \quad 3.75 \le \log T \le 4.20, \tag{A3}$$

$$\text{He I}: \quad 4.20 \le \log T \le 4.75, \tag{A4}$$

$$\text{He II}: \quad 4.55 \le \log T \le 5.10, \tag{A5}$$

$$\text{Fe}: \quad 5.15 \le \log T \le 5.35, \tag{A6}$$

$$\text{deep Fe}: \quad 6.15 \le \log T \le 6.40, \tag{A7}$$

together with an outer surface layer defined by $q = M_r/M_\star \gtrsim 0.99$.

We also evaluate simple envelope diagnostics associated with strange-mode behaviour in luminous, radiation-dominated stars, including large L/M, low outer gas-pressure fraction, short local thermal times, and a large radiative flux fraction (H. Saio et al. 1998, 2013; T. Sonoi & H. Shibahashi 2014). These quantities are used only to flag plausible driving regions. They do not determine the final mode selection, which is based instead on the shell-by-shell work analysis described below.

A.2. *Radial modes*

We begin with linear adiabatic radial pulsations. In Newtonian gravity, writing the radial displacement as $\xi_r = r\eta$, the pulsation equation may be written in self-adjoint form,

$$\frac{d}{dr}\left[A(r)\frac{d\eta}{dr}\right] + \left[B(r) + \omega^2 C(r)\right]\eta = 0, \tag{A8}$$

with

$$A(r) = \Gamma_1 P r^4, \tag{A9}$$

$$B(r) = r^3\frac{d}{dr}[(3\Gamma_1 - 4)P], \tag{A10}$$

$$C(r) = \rho r^4. \tag{A11}$$

Regularity is imposed at the centre, and the outer boundary condition is the vanishing of the Lagrangian pressure perturbation,

$$\Delta P = 0. \tag{A12}$$

We solve for the lowest radial modes by scanning eigenfrequency space, locating sign changes in the surface residual, and refining each root by bisection.

To place the same sequences in a relativistic context, we also solve the general-relativistic radial problem following H. Saio et al. (2024). The equilibrium metric is written as

$$ds^2 = -e^{2a}c^2dt^2 + e^{2b}dr^2 + r^2d\Omega^2, \tag{A13}$$

and the perturbation equations are solved in the variables

$$Y_1 = \frac{\xi_r}{r}, \qquad Y_2 = \frac{\Delta P}{P}, \tag{A14}$$

with

$$\frac{dY_1}{d\ln r} = -\left(3 - \frac{da}{d\ln r}\right)Y_1 - \frac{Y_2}{\Gamma_1}, \tag{A15}$$

$$\frac{dY_2}{d\ln r} = \left[A_{\rm GR} + \omega^2 D_{\rm GR}\right]Y_1 + B_{\rm GR}Y_2. \tag{A16}$$

This GR calculation is used to follow the approach to relativistic softening and instability. The Newtonian modes remain the default basis for the driving and mass-loss estimates described below.

A.3. *Quasi-nonadiabatic driving and mode selection*

The next step is not a full nonadiabatic eigenvalue calculation. Instead, we evaluate local driving and damping terms on the adiabatic eigenfunctions. This provides a transparent picture of where positive work is concentrated and which physical channel is responsible for it.

The local compression implied by the radial displacement is

$$\Delta \ln \rho \approx -\frac{1}{r^2}\frac{d}{dr}\left(r^2 \xi_r\right), \tag{A17}$$

and the associated adiabatic temperature response is

$$\Delta \ln T_{\rm ad} = (\Gamma_3 - 1)\,\Delta \ln \rho. \tag{A18}$$

To measure how effectively a layer can exchange heat over one cycle, we compare the pulsation period P with the local thermal time,

$$t_{\rm th}(r_i) \approx \frac{\sum_{j=i}^{N} C_{V,j} T_j \Delta m_j}{L_\star}, \tag{A19}$$

and define

$$x_{\rm th} = \frac{P}{t_{\rm th}}, \qquad f_{\rm th} = \frac{2x_{\rm th}}{1 + x_{\rm th}^2}. \tag{A20}$$

This weighting peaks when $P \sim t_{\rm th}$. Convective damping is treated in the same spirit by comparing the pulsation period with the local convective turnover time.

Opacity driving is measured through the response of the radiative conductivity,

$$K_{\rm rad} \propto \frac{T^3}{\kappa \rho}, \tag{A21}$$

to adiabatic compression. Using

$$d \ln \kappa = \kappa_T\, d \ln T + \kappa_\rho\, d \ln \rho, \tag{A22}$$

together with the adiabatic relation for $d \ln T$, we obtain

$$\left(\frac{d \ln K_{\rm rad}}{d \ln \rho}\right)_{\rm ad} = (3 - \kappa_T)(\Gamma_3 - 1) - (1 + \kappa_\rho). \tag{A23}$$

Compression increases radiative trapping when this quantity is negative, so the sign-reversed form serves as our local opacity-driving proxy.

For completeness we also monitor the adiabatic sensitivity of the nuclear energy generation rate,

$$\epsilon_{\rm coeff} = \epsilon_T + (\Gamma_3 - 1)\epsilon_\rho. \tag{A24}$$

This term is retained as a diagnostic, but it is not included in the default net-driving sum and is not used as the primary criterion for mode selection.

To represent the outer-envelope contribution, we include a separate surface term that grows when the local layer is radiatively dominated, weakly supported by gas pressure, close to the surface, and dynamically important in the eigenfunction. We interpret this term as a proxy for surface-leakage or strange-mode-like behaviour rather than as a formal strange-mode solution.

The local power densities are therefore written schematically as

$$\dot{p}_\kappa \propto \frac{\rho C_V T}{t_{\rm th}} \left(\Delta \ln T_{\rm ad}\right)^2 f_{\rm rad}\, f_{\rm th}\, \mathcal{T}_\kappa, \tag{A25}$$

$$\dot{p}_{\rm surf} \propto \frac{\rho C_V T}{t_{\rm th}} \left(\Delta \ln T_{\rm ad}\right)^2 \mathcal{S}_{\rm surf}, \tag{A26}$$

$$\dot{p}_{\rm conv} \propto -\frac{\rho C_V T}{t_{\rm th}} \left(\Delta \ln T_{\rm ad}\right)^2 f_{\rm conv}, \tag{A27}$$

where $f_{\rm rad} = L_{\rm rad}/L_{\rm tot}$ after repair, $\mathcal{T}_\kappa$ is the opacity-trapping factor, and $\mathcal{S}_{\rm surf}$ is the surface-driving proxy. The default net driving is

$$\dot{p}_{\rm tot} = \dot{p}_\kappa + \dot{p}_{\rm surf} + \dot{p}_{\rm conv}. \tag{A28}$$

From these local terms we form the global mode energy and driving power,

$$E_{\rm mode} = \int \frac{1}{2} \rho \omega_r^2 \xi_r^2\, dV, \tag{A29}$$

$$\dot{P} = \int \dot{p}_{\rm tot}\, dV, \tag{A30}$$

and define the corresponding growth proxy,

$$\gamma = \frac{\dot{P}}{2E_{\rm mode}}. \tag{A31}$$

The work contributed by each shell over one cycle is

$$W_{{\rm shell},i} = \dot{p}_i\, \Delta V_i\, P. \tag{A32}$$

The mode carried forward at each stored model is chosen by balancing three considerations: positive growth, concentration of positive work in a physically plausible envelope layer, and consistency between that work-producing layer and the candidate region identified from the equilibrium structure.

A.4. *Re-identifying the driving layer*

The outermost zones of luminous stellar models can contain numerically unreliable radiative fractions (A. Maeder & G. Meynet 2000). For that reason, we re-examine the candidate driving region before converting any unstable mode into a mass-loss estimate.

We first rewrite the opacity derivatives in more diagnostic forms. At constant pressure,

$$\left(\frac{\partial \ln \kappa}{\partial \ln T}\right)_P = \kappa_T - \frac{\chi_T}{\chi_\rho}\kappa_\rho, \tag{A33}$$

while along an adiabatic path,

$$\left(\frac{d\ln\kappa}{d\ln T}\right)_{\rm ad} = \kappa_T + \frac{\kappa_\rho}{\Gamma_3 - 1}. \tag{A34}$$

These combinations provide compact measures of whether compression tends to increase radiative trapping.

Where the raw radiative luminosity fraction becomes unphysical, we reconstruct the radiative luminosity from the diffusion form of the temperature gradient,

$$L_{\rm rad,rec} = \frac{16\pi acGM_r T^4 \nabla}{3\kappa P}. \tag{A35}$$

We use the original profile where it remains admissible and substitute the reconstructed value only in problematic cells. The repaired profile is then used to rank the candidate driving zones.

This step does not redefine the stellar model. Its purpose is simply to ensure that the inferred driving layer is physically plausible and not an artifact of a few pathological outer mesh points.

A.5. *Caveat on steady radiative mass loss*

Other forms of mass loss may also operate during SMS evolution and are not excluded here. During brief hot blueward excursions, line-driven winds of the type described by J. S. Vink et al. (2001) could in principle contribute, while on the cool supergiant side one may appeal to empirical prescriptions such as C. de Jager et al. (1988). The difficulty is that these prescriptions are not calibrated for near-Eddington SMS envelopes.

This uncertainty was explored by D. Nandal & S. Chon (2026) for a $Z = 10^{-4}\,Z_\odot$ SMS. Starting from a mid core-H-burning model of $7.3973 \times 10^4\,M_\odot$, they evolved the star without further accretion or collisions until H exhaustion. The de Jager prescription reduced the final mass to $2.3421 \times 10^4\,M_\odot$, implying a total loss of $\sim 5.1 \times 10^4\,M_\odot$, whereas the Vink prescription gave $M_f = 6.2348 \times 10^4\,M_\odot$, implying a loss of only $\sim 1.2 \times 10^4\,M_\odot$. In that test, the Vink-like wind became important only during brief hot contraction phases with $T_{\rm eff} \gtrsim 2.5 \times 10^4\,{\rm K}$. These values should therefore be read only as first-order bounds rather than as robust SMS wind predictions. For that reason, and to isolate the role of discrete pulsational ejection, we do not impose an additional steady radiative-wind prescription in the fiducial calculations. The mass loss discussed here should therefore be read specifically as the pulsation-linked component.

A.6. *From unstable modes to mass loss*

Once a driving layer has been identified, we translate the pulsation diagnostics into a conservative estimate of pulsation-linked mass loss. The coupling is written in terms of a luminosity fraction,

$$f_{\rm coup} = \min\Big[f_{\rm coup,max},\; C_{\rm branch}\, g_P\, \max(W_{\rm metric},\, O_{\rm metric})\, w_{\rm conf}\, b_{\rm ch}\Big] \tag{A36}$$

where $g_P = \gamma P$ is the growth per period, $W_{\rm metric}$ and $O_{\rm metric}$ measure how strongly the inferred driving layer participates in the work budget, $w_{\rm conf}$ is a confidence weight, and $b_{\rm ch}$ allows a modest dependence on the dominant driving channel. The branch-dependent ceiling $f_{\rm coup,max}$ is listed in Table A1. We define

$$\begin{aligned} W_{\rm metric} &= (f_+ f_{|W|})^{1/2}, \\ O_{\rm metric} &= 0.6 f_+ + 0.4\,\min(1,\, 2 f_{|W|}). \end{aligned} \tag{A37}$$

where f_+ is the fraction of the positive work budget arising in the inferred driving layer and $f_{|W|}$ is the corresponding absolute-work fraction.

To reflect the weak binding of the outer envelope, we replace the structural escape speed by an effective escape scale,

$$v_{\rm esc,eff} = v_{\rm esc}\sqrt{f_{\rm bind,eff}}, \qquad v_{\rm esc} = \left(\frac{2GM_\star}{R_\star}\right)^{1/2}, \tag{A38}$$

where $f_{\rm bind,eff}$ is a reduced binding factor derived from the local gas-pressure fraction and radiative support. This is a simple envelope-binding proxy rather than a full dynamical calculation.

The mass-loss rate is then written in energy-limited form,

$$\dot{M} = \frac{2\eta L_{\rm drive}}{v_{\rm esc,eff}^2}, \qquad L_{\rm drive} = f_{\rm coup} L_\star. \tag{A39}$$

Here η is an explicit efficiency factor, varied over low, fiducial, and high branches. Each estimate is capped by the mass accessible above the inferred driving layer, so that the procedure cannot eject more material than is locally available.

The numerical coefficients used in this mapping are collected in Table A1. Surface-dominated cases are allowed to couple more strongly than deeper opacity-driven cases, reflecting the weaker binding of the outermost layers.

This part of the method is necessarily approximate. The present work does not solve nonlinear radiation hydrodynamics, so the mapping from pulsational driving to $\dot{M}$ should be read as a structured estimate rather than as a unique prediction.

Table A1. Branch-dependent parameters used in the pulsation–mass-loss mapping.

Branch family	$C_{\rm branch}$	$f_{\rm coup,max}$	$\eta_{\rm low}$, $\eta_{\rm fid}$, $\eta_{\rm high}$	Accessible mass cap $M_{\rm acc}$
Surface-leakage dominated	6	0.05	0.10, 0.30, 1.00	$\min[M_>, \max(0.5M_>, M_{\rm sh})]$
Opacity-dominated	4	0.02	0.03, 0.10, 0.30	$\min(0.35M_{\rm sh}, M_>)$
Mixed	5	0.03	0.05, 0.15, 0.50	$\min(0.6M_>, 0.6M_{\rm sh} + 0.4M_>)$
Indeterminate	3	0.015	0.03, 0.10, 0.30	$\min(0.25M_{\rm sh}, M_>)$

NOTE—$M_{\rm sh}$ is the mass contained in the inferred driving shell and $M_>$ is the mass above the inner edge of that shell.

A.7. *Finite ejection episodes along each sequence*

A non-zero $\dot{M}$ at a single stored model is not interpreted as a long-lived steady wind. Instead, it marks that stored model as pulsationally active. We do not impose an additional floor in event mass or duration at this grouping stage: models with $\dot{M} = 0$ are treated as quiescent, while contiguous active models are merged into one episode. If only one stored model in a local interval is active, we still assign it a finite duration based on the shorter of the local evolutionary spacing and an intrinsic pulsation timescale,

$$\Delta t_{\rm eff} = \min[\Delta t_{\rm half-gap},\, \max(N_{\rm grow}\tau_{\rm grow},\, N_P P)]\,. \tag{A40}$$

The mass associated with an isolated episode is then

$$\Delta M_{\rm ep} \simeq \dot{M}\,\Delta t_{\rm eff}, \tag{A41}$$

while multi-model episodes are integrated over the sampled active interval. In this bookkeeping, every non-zero $\dot{M}$ estimate in the sampled sequence belongs to exactly one episode, so there is no separate off-episode contribution omitted from the cumulative ejecta mass. In all cases, the low, fiducial, high, and upper-limit branches are kept mutually consistent and are subject to the same reservoir cap.

A.8. *Velocity scales and shell estimates*

Finally, we translate the episode-integrated results into a small set of observer-facing quantities. Alongside the escape speed, we define two characteristic pulsation speed scales,

$$v_{R/P} = \frac{R_\star}{P}, \qquad v_{2\pi R/P} = \frac{2\pi R_\star}{P}, \tag{A42}$$

and the displacement amplitude required for a sinusoidal oscillation to reach escape,

$$A_{\rm crit,esc} = \frac{v_{\rm esc} P}{2\pi R_\star}. \tag{A43}$$

We also report radiative momentum and energy limits,

$$v_{L/c} = \frac{L_\star}{\dot{M}c}, \qquad v_{\rm tir} = \left[\max\left(0, \frac{2L_\star}{\dot{M}} - v_{\rm esc}^2\right)\right]^{1/2}. \tag{A44}$$

These are not predictions of a unique terminal velocity; they are compact measures of whether the inferred event-averaged mass flux is broadly compatible with the available radiative budget.

To estimate where ejected material would lie at a later time, we propagate each episode outward with a simple bracket of launch speeds,

$$v_{\rm low} = v_{R/P}, \qquad v_{\rm high} = v_{2\pi R/P}. \tag{A45}$$

For an episode evaluated at time $t_{\rm ref}$, with start and end times $t_{\rm start}$ and $t_{\rm end}$, the inner and outer shell radii are

$$r_{\rm in} = \max[r_{\rm launch}, v_{\rm low}(t_{\rm ref} - t_{\rm end})_+]\,, \tag{A46}$$

$$r_{\rm out} = \max[r_{\rm in}, r_{\rm launch} + v_{\rm high}(t_{\rm ref} - t_{\rm start})_+]\,, \tag{A47}$$

where $(x)_+ = \max(x, 0)$. From these we define the shell thickness,

$$\Delta R = r_{\rm out} - r_{\rm in}, \tag{A48}$$

and the thin-shell surface density,

$$\Sigma_{\rm sh}(r) \simeq \frac{M_{\rm sh}}{4\pi r^2}, \tag{A49}$$

which gives an optical-depth proxy,

$$\tau(r) \simeq \kappa\,\Sigma_{\rm sh}(r). \tag{A50}$$

For the shell diagnostics quoted in the main text, we evaluate this proxy at the inner edge, outer edge, and geometric-mean radius of the shell, giving $\tau_{\rm in} = \tau(r_{\rm in})$, $\tau_{\rm out} = \tau(r_{\rm out})$, and $\tau_{\rm geo} = \tau(\sqrt{r_{\rm in} r_{\rm out}})$. Unless stated otherwise, we adopt a constant electron-scattering opacity $\kappa = 0.34\,{\rm cm^2\,g^{-1}}$ for these order-of-magnitude estimates.

A.9. *Composition of the ejected layers*

For selected episodes we also examine the composition of the outer layers implicated by the inferred mass loss. If an episode ejects a mass $\Delta M_{\rm ep}$, the corresponding outer mass depth is

$$\Delta q_{\rm ep} = \frac{\Delta M_{\rm ep}}{M_\star}. \tag{A51}$$

We then inspect the abundance profiles over the outer mass interval associated with that depth. This procedure does not introduce any additional mixing or nucleosynthesis; it simply identifies the composition of the layers that would be sampled by an ejection of the inferred depth. These abundance diagnostics are used only as a post-processing aid when interpreting the composition of the expelled material. The abundance ratios reported in the main text are computed from the integrated shell masses over that selected interval and are quoted as shell-averaged logarithmic number ratios.

A.10. *Metallicity dependence of the shell and ejecta diagnostics*

Table A2 shows that all five Phase XVI sequences end with nearly the same final mass, $M_{\rm f} \simeq 10^5\,M_\odot$, but not with the same late-time pulsational behaviour. The main metallicity dependence appears instead in the number of eruptive episodes, the amount of mass removed, the compactness of the terminal envelope, and the chemistry of the expelled shell. The central result is already clear from the table itself: pulsation-driven shell ejection is not unique to the $Z = 10^{-2}\,Z_\odot$ model, but is present from Pop III to $10^{-2}\,Z_\odot$.

The non-monotonic behaviour with metallicity is physically expected. In luminous stars, strange-mode instability is not controlled by a single opacity feature. Classical stability calculations identify one family associated with He ionization and another associated with heavy-element opacity enhancement (M. Kiriakidis et al. 1993). The first can remain important even at very low metallicity, while the second becomes stronger as metal opacity increases. Near-Eddington envelopes can therefore remain susceptible to inflation and strange-mode driving across a wide metallicity range. The existence of pulsations is thus generic, but their timing, multiplicity, and ejecta yield need not vary smoothly with Z.

This interpretation helps explain the burst statistics in Table A2. The $Z = 10^{-3}\,Z_\odot$ sequence produces the largest number of fiducial episodes, $N_{\rm ep} = 28$, whereas the $Z = 10^{-5}\,Z_\odot$ model yields the largest cumulative ejecta mass, $\Delta M_{\rm ej} = 6.26 \times 10^3\,M_\odot$ on the fiducial branch and $1.47 \times 10^4\,M_\odot$ on the upper branch. By contrast, the $Z = 10^{-2}\,Z_\odot$ case shows only four fiducial episodes and the smallest total ejected mass, $\Delta M_{\rm ej} = 4.80 \times 10^2\,M_\odot$. Frequent bursting and efficient mass removal are therefore not the same thing.

The terminal structural quantities in Table A2 divide the grid into two broad regimes. The Pop III model is the clear outlier: it ends much hotter and more compact, with $\log T_{{\rm eff},f} = 4.872$ and $v_{\rm esc,last} = 7731\,{\rm km\,s^{-1}}$. The metal-enriched models instead cluster near $\log T_{{\rm eff},f} \simeq 4.0$ and $v_{\rm esc,last} \simeq 1200$–$1600\,{\rm km\,s^{-1}}$, while all retain $\Gamma_{{\rm Edd},f} \approx 1$. This suggests that the decisive metallicity effect is not a large change in L/M itself, but a change in how that near-Eddington luminosity is expressed in the envelope structure. Once the metal-enriched models settle into cooler and less tightly bound envelopes, strange-mode driving can more easily expel optically important outer material.

The shell quantities strengthen the same conclusion. Across the entire grid, the shell identified in Table A2 remains compact and optically thick, with $\tau_{\rm es}$ between $\sim 7.4 \times 10^2$ and 1.3×10^4. Thus, the production of a dense inner shell is not restricted to one metallicity. What changes with Z is the balance between total ejecta mass, shell compactness, and terminal stellar state. In this sense, the $Z = 10^{-2}\,Z_\odot$ model is not special because it maximizes the ejected mass. It is special because it provides the clearest LRD analogue, combining the coolest enriched terminal state with a compact optically thick shell.

The chemical columns of Table A2 add a second strong conclusion. The Pop III shell is chemically distinct, with very large positive $\log(C/O)$ and $\log(N/O)$, marking the extreme primary-processing limit. Among the metal-enriched models, the shells remain H/He dominated, but the detailed CNO pattern changes with both metallicity and ejection depth. The $Z = 10^{-5}\,Z_\odot$ and $Z = 10^{-4}\,Z_\odot$ models show appreciable branch sensitivity, especially in $\log(N/O)$, whereas the $Z = 10^{-3}\,Z_\odot$ and $Z = 10^{-2}\,Z_\odot$ cases give robust nitrogen-rich shells. For the $Z = 10^{-3}\,Z_\odot$ model, $\log(N/O) = 0.334$–0.359. For the $Z = 10^{-2}\,Z_\odot$ model, the final-shell values are $\log(N/O) \simeq 0.13$ and 0.10 for the fiducial and upper branches, respectively, consistent with the main-text shell analysis. The He/H ratio varies much less than the CNO ratios, confirming that these events expel outer H/He envelope material rather than exposing a fully processed core. Among the metal-enriched models, Ne/O is also more stable than N/O, which makes N/O the sharper abundance discriminator.

Taken together, Table A2 shows that late pulsational shell ejection is a generic feature of our SMS models, not a peculiarity of the $Z = 10^{-2}\,Z_\odot$ sequence. Metallicity does not decide whether such shells occur at all; it regulates how they occur. Lower and intermediate metallicities can eject more total mass and often do so through more numerous episodes, while finite-metallicity models near 10^{-3}–$10^{-2}\,Z_\odot$ produce the clearest combination of a cool inflated terminal state, a compact optically thick shell, and an observationally useful nitrogen-rich composition.

A.11. *GR stability analysis*

At each stellar-evolution timestep, we assess the approach to collapse with three complementary GR stability criteria: the full linear adiabatic GR analysis of H. Saio et al. (2024), the post-Newtonian instability estimate of L. Haemmerlé (2021a), and the GR radial-stability method of C. Nagele et al. (2022). The first two define the main evolutionary instability point used in the stellar-evolution analysis, while the Nagele et al. criterion is also used to select the snapshot for the hydrodynamic follow-up. In practice, this criterion identifies a slightly earlier unstable model and avoids remapping a profile with an artificially steep outer pressure gradient.

For the direct GR radial-stability check, we solve the Chandrasekhar pulsation equation (**?**),

$$e^{-2a-b}\frac{d}{dr}\left[\frac{e^{3a+b}\Gamma_1 P}{r^2}\frac{d}{dr}\left(e^{-a}r^2\xi\right)\right]-\frac{4}{r}\frac{dP}{dr}\xi + e^{-2a+2b}\omega^2(P+\rho c^2)\xi-\frac{8\pi G}{c^4}e^{2b}P(P+\rho c^2)\xi - \frac{1}{P+\rho c^2}\left(\frac{dP}{dr}\right)^2\xi=0, \tag{A52}$$

which has previously been applied to numerical SMS models (L. Haemmerlé 2021a; C. Nagele et al. 2022). Here $\rho=\rho_{\rm baryon}(1+\epsilon/c^2)$ is the relativistic density, a and b are metric coefficients, and $\xi(r)e^{i\omega t}$ is the radial displacement. The solutions form a discrete mode sequence with $\omega_n^2<\omega_{n+1}^2$. Instability therefore occurs once the fundamental mode satisfies $\omega_0^2<0$. We have cross-checked this criterion against the hydrodynamic collapse calculations described below.

A.12. *1D GR hydrodynamic follow-up*

Once an unstable snapshot is selected with the GR stability analysis above, we remap the GENEC structure to a 1D Lagrangian GR hydrodynamics code (C. Nagele et al. 2020). The code includes a 52-isotope nuclear network and thermal-neutrino cooling (C. Nagele et al. 2021). We use this calculation as a consistency check on the linear stability analysis and to verify the final collapse outcome of the unstable SMS.

Figure 6 illustrates the collapse dynamics in the baseline run. The velocity profiles are initially close to homologous, with inward motion across most of the star. At later times, the inner regions accelerate more strongly than the outer layers, and the collapse becomes increasingly centrally concentrated as black-hole formation approaches. In the baseline non-rotating calculation, we find collapse rather than disruption.

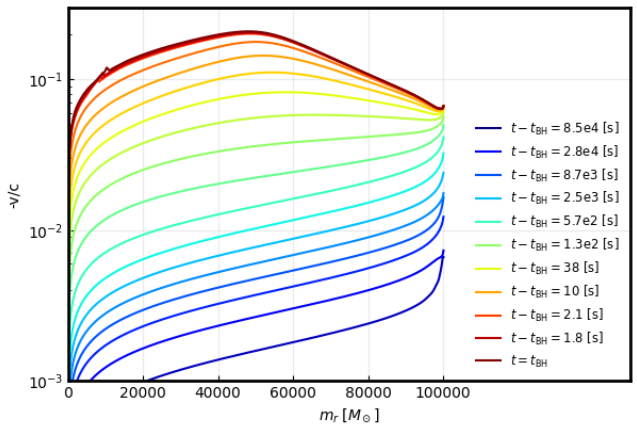

Figure 6. Radial velocity profiles in units of c as a function of enclosed mass coordinate for selected times in the 1D GR hydrodynamic follow-up of the unstable SMS model. The collapse is initially close to homologous, with inward motion across most of the star, and later becomes increasingly centrally concentrated as black-hole formation approaches.

A.13. *Why a truly cool hydrostatic photosphere is not required*

The shell-reprocessing picture above offers a natural explanation for the low apparent continuum temperatures inferred for some LRDs. It also avoids a difficulty faced by models in which the central source itself has a true hydrostatic photosphere at $T_{\rm eff}\sim 3000$–4000 K.

A stellar photosphere in that temperature range should resemble a cool supergiant atmosphere. Such spectra are expected to show strong molecular absorption bands, especially from TiO, and often also from C_2 and CN (E. M. Levesque 2017). These features should remain visible even at low spectral resolution. Even red supergiants with weak CN still show clear TiO structure (P. Guhathakurta et al. 2025). By contrast, a hotter source seen through an expanding dense shell can produce a much cooler continuum without requiring the underlying source itself to be a 3000–4000 K star.

Dense shells also provide a natural route to reddening. A moderately reddened $T_{\rm eff}\sim 7000$ K atmosphere can resemble a cooler atmosphere without strong molecular bands in low-resolution data. This helps explain why continuum-based temperature estimates alone may bias the source toward artificially low values. The low-redshift LRD analog $J1025+14$ supports this caution. Its continuum appears very cool, yet its absorption features imply substantially higher surface temperatures (R. Lin et al. 2025; X. Ji et al. 2026).

Table A2. Summary of the five $10^5\,M_\odot$ Phase XVI sequences as a function of metallicity. Listed are the number of fiducial ejection episodes, the total integrated ejected mass $\Delta M_{\rm ej}$, the largest single-episode ejecta mass $M_{\rm ep,max}$, the final stellar mass $M_{\rm f}$, the final effective temperature $\log T_{\rm eff,f}$, the final Eddington factor $\Gamma_{\rm Edd,f}$, the terminal escape speed $v_{\rm esc,last}$, the upper launch-speed proxy $v^{+}_{\rm launch}$, and the characteristic radius $R_{\rm sh}$ and electron-scattering optical depth $\tau_{\rm es}$ of the most relevant shell. The final columns give the integrated ejecta abundance ratios $\log(C/O)$, $\log(N/O)$, $\log$(He/H), and $\log$(Ne/O) as logarithmic number ratios. For cells with two entries, the upper and lower values correspond to the fiducial and upper-limit cases, respectively.

$Z/Z_\odot$	$N_{\rm ep}$	$\Delta M_{\rm ej}$ $[M_\odot]$	$M_{\rm ep,max}$ $[M_\odot]$	$M_{\rm f}$ $[M_\odot]$	$\log T_{\rm eff,f}$	$\Gamma_{\rm Edd,f}$	$v_{\rm esc,last}$ $[{\rm km\,s^{-1}}]$	$v^{+}_{\rm launch}$ $[{\rm km\,s^{-1}}]$	$R_{\rm sh}$ [pc]	$\tau_{\rm es}$	$\log(C/O)$	$\log(N/O)$	$\log$(He/H)	$\log$(Ne/O)
		2004.6	976.6								2.805	3.542	-1.083	-9.446
0	14	2711.8	1004.8	100662	4.872	0.977	7731	5058	1.4e-05	1.26×10^4	2.797	3.538	-1.083	-9.440
		6262.1	755.9								-0.756	-0.109	-1.048	-0.542
10^{-5}	24	14656.4	1000.1	100888	4.018	1.005	1432	1291	1.2e-04	2.30×10^3	-0.832	0.145	-0.917	-0.528
		1854.8	990.5								-0.385	-0.519	-1.077	-0.545
10^{-4}	14	3336.2	1000.9	100653	4.058	1.006	1574	1382	5.3e-05	2.25×10^3	-0.562	-0.253	-1.057	-0.535
		4827.4	998.9								-0.249	0.334	-0.659	-0.551
10^{-3}	28	7196.6	999.2	100185	4.066	0.994	1555	29656	9.3e-05	742.71	-0.246	0.359	-0.630	-0.551
		479.9	348.0								-0.232	0.13	-0.966	-0.505
10^{-2}	4	1039.6	599.9	100254	3.965	0.980	1176	1358	1.5e-04	2.46×10^3	-0.263	0.10	-0.969	-0.505

Note—For cells with two entries, the upper and lower values correspond to the fiducial and upper-limit cases, respectively. $R_{\rm sh}$ is in pc. Abundance ratios are logarithmic number ratios.